

Morphometric Analysis of Aqueous Humor Outflow Structures with Spectral-Domain Optical Coherence Tomography

Andrew W. Francis,¹ Larry Kagemann,^{2,3} Gadi Wollstein,² Hiroshi Ishikawa,^{2,3} Steven Folz,⁴ Darryl R. Overby,^{4,5} Ian A. Sigal,^{2,3,6} Bo Wang,² and Joel S. Schuman^{2,3,6,7}

PURPOSE. To describe morphometric details of the human aqueous humor (AH) outflow microvasculature visualized with 360-degree virtual castings during active AH outflow in cadaver eyes and to compare these structures with corrosion casting studies.

METHODS. The conventional AH outflow pathways of donor eyes ($n = 7$) and eyes in vivo ($n = 3$) were imaged with spectral-domain optical coherence tomography (SD-OCT) and wide-bandwidth superluminescent diode array during active AH outflow. Digital image contrast was adjusted to isolate AH microvasculature, and images were viewed in a 3D viewer. Additional eyes ($n = 3$) were perfused with mock AH containing fluorescent tracer microspheres to compare microvasculature patterns.

RESULTS. Observations revealed components of the conventional outflow pathway from Schlemm's canal (SC) to the superficial intrascleral venous plexus (ISVP). The superficial ISVP in both our study and corrosion casts were composed of interconnected venules (10–50 μm) forming a hexagonal meshwork. Larger radial arcades (50–100 μm) drained the region nearest SC and converged with larger tortuous vessels (>100 μm). A 360-degree virtual casting closely approximated corrosion casting studies. Tracer studies corroborated our

findings. Tracer decorated several larger vessels (50–100 μm) extending posteriorly from the limbus in both raw and contrast-enhanced fluorescence images. Smaller tracer-labeled vessels (30–40 μm) were seen branching between larger vessels and exhibited a similar hexagonal network pattern.

CONCLUSIONS. SD-OCT is capable of detailed morphometric analysis of the conventional outflow pathway in vivo or ex vivo with details comparable to corrosion casting techniques. (*Invest Ophthalmol Vis Sci.* ;53:5198–5207) DOI:10.1167/iops.11-9229

Elevated intraocular pressure (IOP) is a major risk factor for glaucoma disease progression, and presently all treatments are aimed at reducing IOP. The limbus is the anatomical region containing aqueous humor (AH) outflow structures from the anterior chamber (AC), and it maintains IOP within the normal physiologic range through a balance between AH production and outflow.¹ Aberrations to the aqueous outflow pathway can increase AH outflow resistance, resulting in impeded AH outflow and elevation of IOP, ultimately leading to an increased risk of glaucoma.^{2,3}

The earliest imaging studies intended to elucidate the normal structure of limbal outflow vasculature utilized biomicroscopic examination in situ or in whole enucleated eyes with or without the use of contrast.^{4,5} These early studies established that AH flowed from the anterior chamber (AC) to Schlemm's canal (SC) and reached the superficial limbal vasculature via connecting vessels. Further studies have shown that the majority of AH leaves the eye through limbal structures that comprise the conventional pathway (trabecular meshwork, Schlemm's canal, collector channels, aqueous venous plexus, and episcleral veins) (Fig. 1). The aqueous venous plexus is a complex network that includes the deep, midlimbal, and perilimbal scleral plexuses leading to scleral veins or Ascher's aqueous veins, which bypass this tortuous pathway and connect directly from SC to the episcleral veins.^{1,6–9}

Spectral-domain optical coherence tomography (SD-OCT) and ultrasound imaging of the anterior segment have produced cross-sectional images of the drainage system, but these do not yield sufficient visualization to ascertain the condition or density of the complex three-dimensional (3D) structures of the AH outflow system.^{10–12} SD-OCT rapidly quantifies tissue reflectance in 3D cubes at speeds up to 512,000 axial scans (A-scans) per second.^{13,14} Coupling the high scanning speed with ultrahigh resolution, it is possible to visualize the individual components of the AH outflow system from the anterior chamber throughout the system of aqueous veins in the living human eye.¹¹ In an earlier study visualizing the gross morphology of the AH outflow channels, a previously

From the ¹Department of Ophthalmology, Boston University School of Medicine, Boston, Massachusetts; the ²Department of Ophthalmology, UPMC Eye Center, Eye and Ear Institute, Ophthalmology and Visual Science Research Center, University of Pittsburgh School of Medicine Pittsburgh, Pennsylvania; the ³Department of Bioengineering, Swanson School of Engineering, Pittsburgh, Pennsylvania; ⁴The McGowan Institute for Regenerative Medicine, University of Pittsburgh School of Medicine, Pittsburgh, Pennsylvania; the ⁵Fox Center for Vision Restoration of UPMC and the University of Pittsburgh, Pittsburgh, Pennsylvania; the ⁶Department of Biomedical Engineering, Tulane University, New Orleans, Louisiana; and the ⁷Department of Bioengineering, Imperial College, London.

Supported in part by National Institutes of Health contracts R01-EY13178 and P30-EY08098 (Bethesda, MD), the National Glaucoma Research Program of the American Health Assistance Foundation, the Eye and Ear Foundation (Pittsburgh, PA), and unrestricted grants from Research to Prevent Blindness (New York, NY).

Submitted for publication December 2, 2011; revised February 9, 2012; accepted February 10, 2012.

Disclosure: **A.W. Francis**, None; **L. Kagemann**, None; **G. Wollstein**, None; **H. Ishikawa**, None; **S. Folz**, None; **D.R. Overby**, None; **I.A. Sigal**, None; **B. Wang**, None; **J.S. Schuman**, P

Corresponding author: Joel S. Schuman, UPMC Eye Center, Department of Ophthalmology, University of Pittsburgh School of Medicine, 203 Lothrop Street, Eye and Ear Institute, Suite 816, Pittsburgh, PA 15213; schumanjs@upmc.edu.

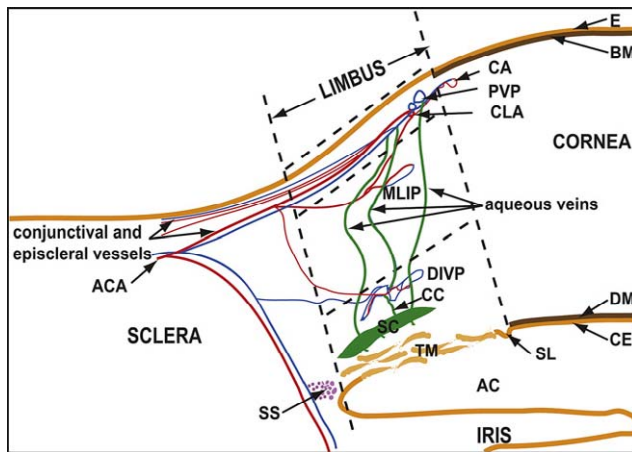


FIGURE 1. A drawing showing the general organization of the aqueous and blood vessels of the ocular limbus. The superficial limbus is indicated between the upper and middle horizontal dashed lines, the mid limbus lies between the middle and lower horizontal dashed lines, and the deep limbus lies below the lower horizontal dashed line. AC, anterior chamber; ACA, anterior ciliary artery; CA, corneal arcades; BM, Bowman's membrane; CC, collector channel; CE, corneal endothelium; CLA, circular limbal artery; DM, Descemet's membrane; DIVP, deep intrascleral venous plexus; E, ocular surface epithelium; MLIP, midlimbal intrascleral plexus; PVP, perilimbal venous plexus; SC, Schlemm's canal; SL, Schwalbe's line; SS, scleral spur; TM, trabecular meshwork. Reprinted from *Experimental Eye Research*, Vol. 91, Issue 2, E. L. van der Merwe and S.H. Kidson, Advances in imaging the blood and aqueous vessels of the ocular limbus, pages 118–126, 2010, with permission from Elsevier.

undescribed fine meshwork structure was observed in the AH capillary networks.¹⁵ The purpose of the present study was to create 3D visualizations of the AH outflow vasculature to describe morphometric details of microvasculature visible with an improved SD-OCT processing schema and to compare microvascular morphologies to those found in corrosion casting studies.

MATERIALS AND METHODS

Human cadaver eyes with no history of eye disease, trauma, or ocular surgery other than cataract were obtained from the Florida Eye Bank (Miami, FL) and the Center for Organ Recovery and Education (Pittsburgh, PA). The Committee for Oversight of Research Involving the Dead of the University of Pittsburgh approved the study. Consent for the use of all tissues for research was obtained by the individual agency responsible for harvesting and supplying the tissue. In addition, in vivo healthy eyes were recruited and imaged from the staff of the University of Pittsburgh. The living subject portion of the study was conducted in accordance with the tenets of the declaration of Helsinki and the Health Insurance Portability and Accountability Act. The institutional review board of the University of Pittsburgh approved the study. All subjects gave written informed consent prior to participation in the study.

Tissue Preparation and Perfusion

Our methodology for tissue preparation and perfusion has been described in detail in a previous manuscript.^{15–17} Seven cadavers and three living eyes were imaged (Table 1). The time window between death and fixation was less than 24 hours. Perfusion pressure is the difference between the AC pressure and the episcleral pressure and can be considered the driving force for AH outflow. In this study, a normal episcleral venous pressure of 8 mm Hg in living eyes was

TABLE 1. Seven Eyes Were Imaged

Eye	Condition	Anterior Chamber Pressure
1, 2	Intact	20 mm Hg
3	Conjunctiva and Tenon's capsule removed	20 mm Hg
4–7	Conjunctiva and Tenon's capsule removed	10 mm Hg
8–10	Healthy in vivo	NA

The presence of the superficial tissues and anterior chamber pressure varied. NA, not available.

assumed.¹⁸ The first two intact eyes were perfused with an anterior chamber pressure of 20 mm Hg. Since the episcleral venous pressure in a cadaver eye is approximately 0 mm Hg, an anterior chamber pressure of 20 mm Hg produced a perfusion pressure equivalent to an IOP of 28 mm Hg in a living eye. An anterior chamber pressure of 10 mm Hg yielded a perfusion pressure equivalent to an IOP of 18 mm Hg in a living eye. Four eyes were perfused and imaged at 10 mm Hg and then were perfusion fixed at 10 mm Hg. One of these eyes was first imaged at a perfusion pressure of 0 mm Hg. One eye was perfused and imaged at 20 mm Hg. After imaging, it was perfusion fixed at 20 mm Hg.

To validate our SD-OCT images, additional eyes ($n = 3$) from ostensibly nonglaucomatous donors were obtained from the National Disease Research Interchange. Eyes were perfused with mock aqueous humor containing fluorescent tracer microspheres (Invitrogen-Molecular Probes, Eugene, OR; 0.2 μm ; 0.002% volume-to-volume) at 7 or 15 mm Hg. Each eye was perfusion fixed with 4% paraformaldehyde and sectioned into quadrants. The tracer labeling pattern within the episcleral vessels was imaged in each quadrant using an epifluorescent microscope (Nikon TE-2000E, Tokyo, Japan) outfitted with a 1 \times objective.

SD-OCT Imaging and Image Processing

Our methodology for SD-OCT imaging has been described in detail in previous manuscripts.^{15,19} An SD-OCT optics engine (Bioptigen, Research Triangle, Durham, NC) was coupled with a wide-bandwidth superluminescent diode array (870-nm center wavelength, 200-nm bandwidth; model Q870; Superlum Ltd, Dublin, Ireland). For each eye, a set of 36 individual radial scan sets were acquired; each clock hour was imaged at its center and offset to the left and right. The density of the 3D volume scan protocol consisted of 512 \times 512 axial scans (A-scans) probing a 2 \times 3 mm (radial \times transverse) area of tissue. The final 2 \times 3 area of tissue image was converted to a uniform 4 \times 4 mm image. One living eye was scanned using Doppler so that velocity could be used to distinguish large blood vessels from large AH outflow vessels.

Raw SD-OCTs were averaged with a floating 5 \times 5 pixel transverse kernel, consisting of five pixels in each of five adjacent frames, and were used to produce an average dataset, using customized software of our own design. Further image processing was performed using Fiji (Fiji 1.44, <http://fiji.sc/wiki/index.php/Fiji>). Images were imported in raw .bog file format after the 5 \times 5 \times 5 “rolling average” function was completed. A “Gaussian blur” filter was then applied before converting the image to 8 bit format. Images were resampled to provide a 1:1:1 voxel aspect ratio in three dimensions; from 512 \times 512 \times 1024 to 342 \times 512 \times 342 for each 2 \times 3 \times 2-mm volume. Images were then inverted so that the black collector channels appeared as white structures and the Fiji “subtract background” filter was applied.

Contrast enhancement was applied to both SD-OCT and microsphere fluorescence images. An “Enhance Local Contrast” filter was applied, which brightens the existing contrast of each slice in a stack according to the optimal for each individual slice and the pixels within the slice. Enhancing contrast increases both the contrast associated with vessels and also the contrast of unwanted noise (Fig. 2). Manual contrast adjustment followed in both SD-OCT and fluorescence images until an optimal balance was achieved. The SD-OCT 3D volumes were

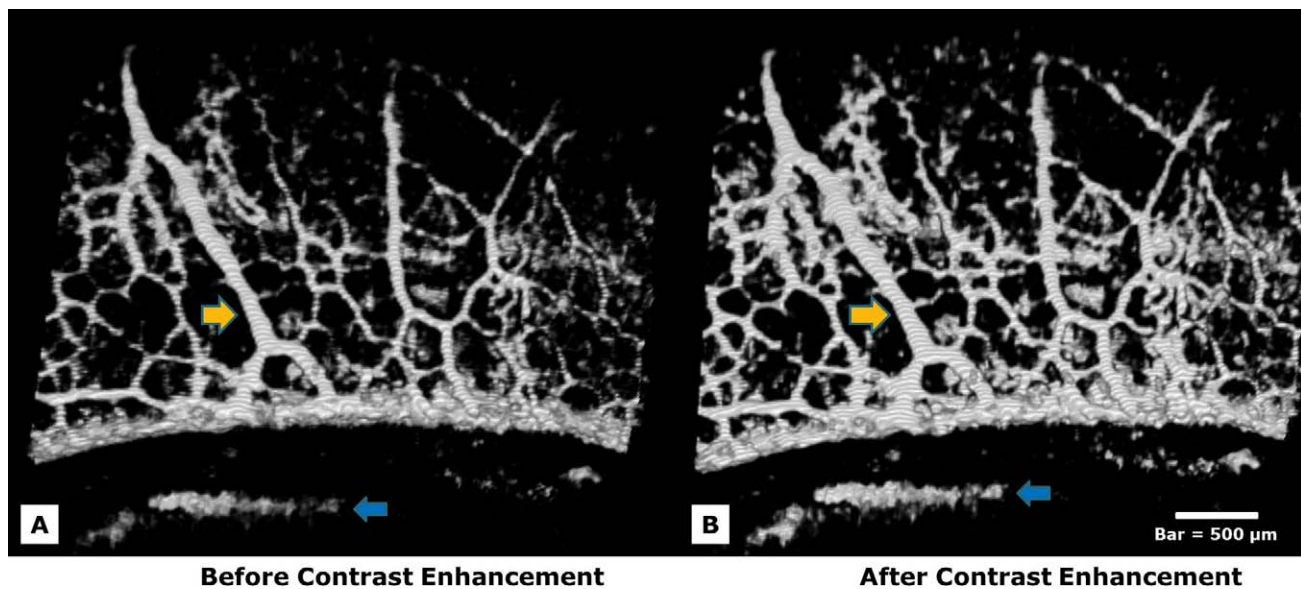


FIGURE 2. Several straight radial arcades draining vessels perpendicular to the limbal margin are shown (*yellow arrows*). Contrast enhancement was applied to SD-OCT images to increase image clarity. Enhancing contrast significantly increased both the contrast associated with vessels (*yellow arrows*) and also the contrast of noise (*blue arrows*). (A) An image is shown prior to contrast enhancement. (B) The same image is shown after contrast enhancement. Manual contrast adjustment followed in both SD-OCT and fluorescence images until an optimal balance was achieved. Bar = 500 μm .

rendered using the Fiji 3D viewer plug-in. Vessel diameters were estimated in the $4 \times 4\text{-mm}$ scan by measuring the number of pixels within the vessels and estimating their cross-sectional size. For example, each pixel in the horizontal direction corresponds to a width of (4 mm/total pixels in x direction). The “Analyze, Set scale” function was used to convert pixel size into a metric distance, which was then measured with a line tool.

RESULTS

Direct observations of the SD-OCT images revealed components of the superficial ISVP, connecting aqueous veins, and SC in all eyes. Confirmation of location was obtained by matching vascular patterns seen in the 3D virtual corrosion cast with corresponding B-scan cross-sectional images (Figs. 3A–D). The

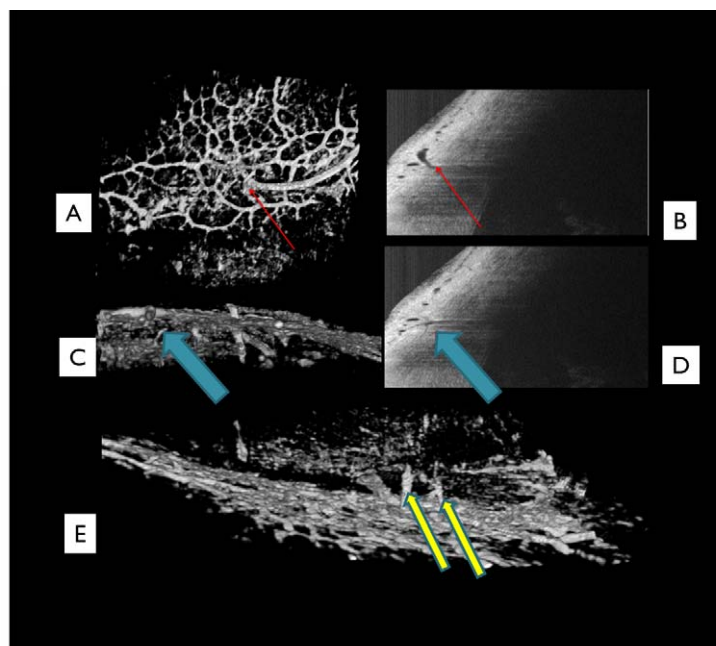


FIGURE 3. The superficial venous plexus visualized was composed of a series of small interconnected venules between 25 and 100 μm in diameter with many interconnecting branch points forming a dense vascular hexagonal meshwork (A). *Red arrows* indicate a vessel seen on the virtual casting (A) and its corresponding location in B-scan (B). *Blue arrows* indicate a suspected aqueous vein (C) descending from the superficial ISVP to the midlimbal ISVP and its corresponding location in B-scan (D). *Yellow arrows* indicate two suspected aqueous veins seen in this 180 degree rotated virtual casting image (E).

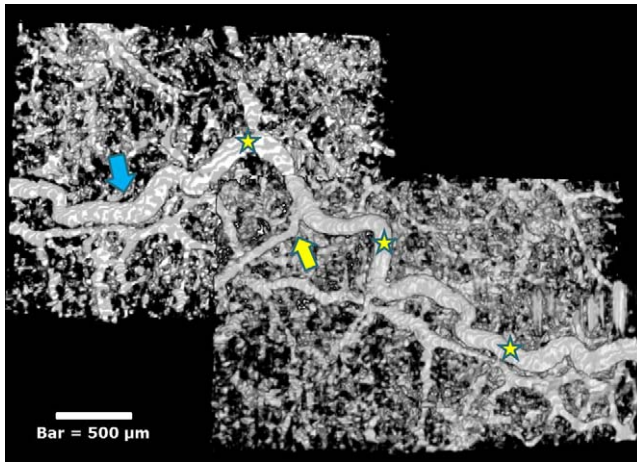


FIGURE 4. The path of a large tortuous vein is shown after image contrast enhancement (*yellow stars*). A smaller venous structure is shown draining into the larger tortuous vein (*yellow arrow*). The smallest visualized structures, between 15 and 30 μm , form a dense vasculature mesh surrounding the large vessels. Light and dark striations of unknown origin are also seen (*blue arrow*). Bar = 500 μm .

superficial venous plexus visualized was composed of a series of small, interconnected venules 10 to 50 μm in diameter with many interconnecting branch points forming a dense vascular hexagonal meshwork (Fig. 3A). Vessels approaching the size of capillaries ($<10 \mu\text{m}$) were assumed to be present but were poorly visualized. When viewed along the long horizontal axis, venous structures are seen to descend into the deeper limbus and form branches into midlimbal venous plexus structures, which are also visible in B-scan cross-sections (Figs. 3C, 3D).

The venous plexus was drained posteriorly by several larger veins forming a series of radial arcades. These vessels are 50 to 100 μm in diameter and progressively converge into larger vessels moving posteriorly away from the image margin and SC (Fig. 2, yellow arrows). These vessels converge with larger, more tortuous vessels, greater than 100 μm in diameter, which were rarely observed (Fig. 4, yellow arrow). Unlike the radial arcades, large tortuous veins do not travel in a consistent direction in relation to the image margin. It is unclear, from these visualizations, where these large tortuous vessels

terminate or converge. An unusual striation was also observed in our 3D virtual castings, as a series of light and dark stripes after contrast enhancement on both vessels and noise. This striation became more distinct after repeated contrast enhancement (Figs. 2, 4).

A similar vascular pattern was observed in tracer-perfused eyes (Fig. 6), where tracer was found to decorate several larger vessels (50–100 μm) extending posteriorly from the limbus in both raw and contrast-enhanced (Fig. 5) fluorescence images. Smaller tracer-labeled vessels (30–40 μm) were often seen branching between the larger vessels, occasionally exhibiting a hexagonal network pattern (Figs. 5, 6). There was significant variability in tracer labeling around the episcleral limbus, with intense labeling observed in some quadrants, while other quadrants of the same eye exhibited very little label.

Nasal and temporal *in vivo* scans in three eyes confirmed the vessel morphology observed in cadaver eyes. All three previously described vascular structures (venules, radial veins, and large tortuous veins) were visualized *in vivo* (Fig. 7). Few significant differences were observed between *in vivo* and *ex vivo* virtual castings. Structures *in vivo* appeared less consistent in diameter than *ex vivo* (Fig. 8). Doppler studies were performed on one eye *in vivo* to confirm flow through a large tortuous venous structure (Fig. 9). The high velocity signature of this vessel, compared to the low velocities within aqueous humor outflow vasculature, suggest that this was a blood vessel.

Qualitative assessment of vasculature density showed dense concentrations in the nasal and temporal position in all eyes, forming branching arcades that drained into progressively larger vessels at increasing distances from the limbus. This *in vivo* observation supported previous *ex vivo* injected silicone and neoprene physical corrosion casting studies (Figs. 10, 11).^{7–9,20,21}

DISCUSSION

We present the first SD-OCT 360-degree virtual casting of outflow microvasculature comprising the ISVP, connecting aqueous veins, and components of SC. Our methodology, in contrast to physical corrosion casting, is completely noninvasive and may be performed in living human eyes. Previous methods used to image the limbal vessels include serial sections with or without dye, ultrathin sections, microvascular perfusion with plastics, rubber, or silicone and corrosion

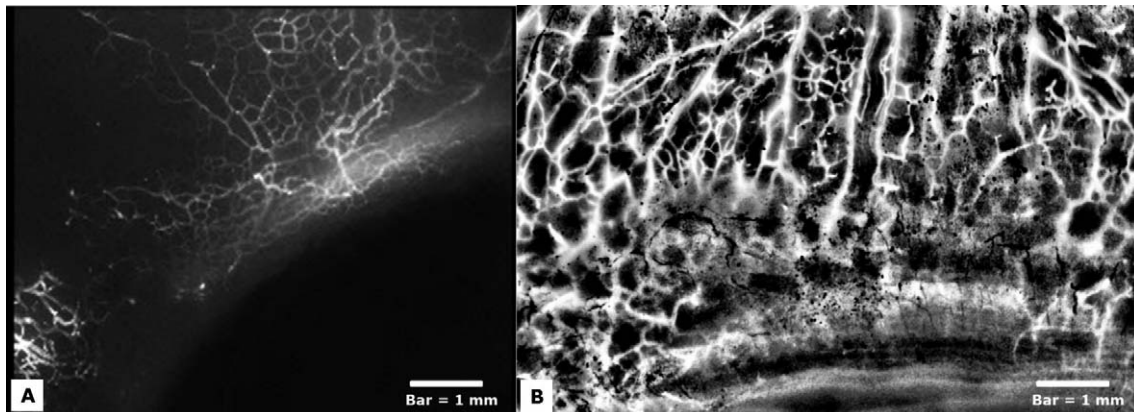


FIGURE 5. (A) Fluorescence imaging of eyes perfused with fluorescent microspheres (diameter = 0.2 μm) revealed a meshwork-like network of aqueous humor outflow veins with significant variability in tracer labeling observed near the episcleral limbus. Bar = 1 mm. (B) Local histogram equalization and background subtraction filters applied to a fluorescence image reveals a meshwork of outflow vasculature extending into the outflow vascular tree down to Schlemm's canal. Bar = 1 mm.

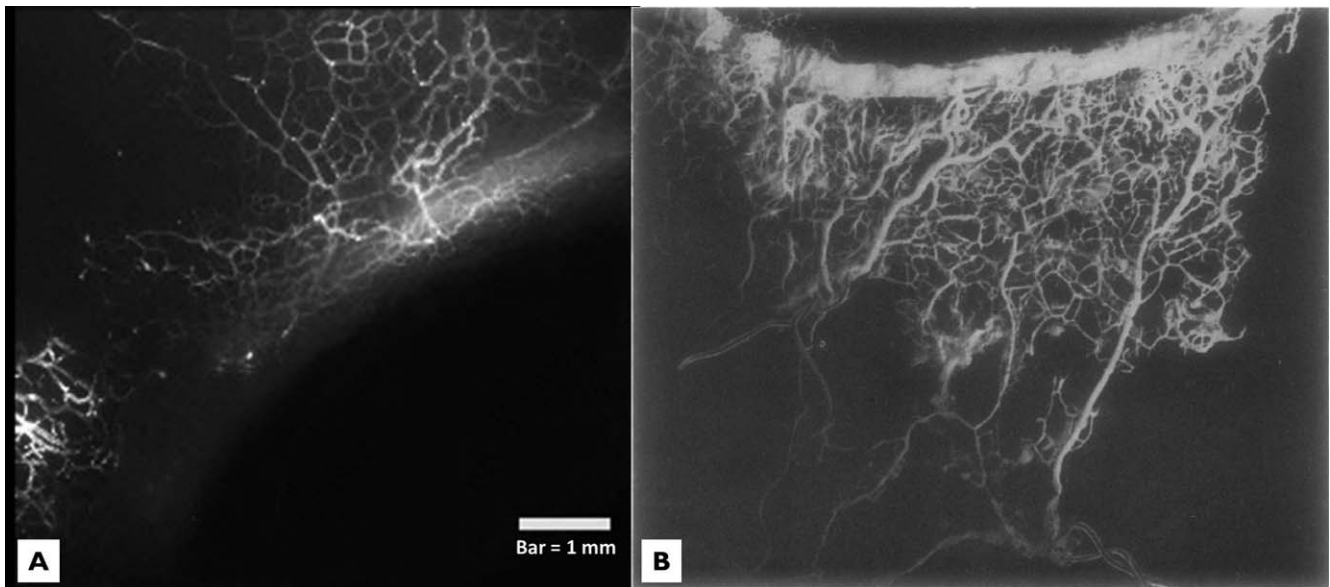


FIGURE 6. (A) Aqueous humor outflow microvasculature perfused with fluorescent microspheres is compared with (B) a neoprene corrosion casting of Schlemm's canal. A similar network of aqueous humor outflow veins is visible extending posteriorly away from Schlemm's canal in both images. Bar = 1 mm. Adapted by permission from BMJ Publishing Group Ltd. Anatomical study of Schlemm's canal and aqueous veins by means of neoprene casts: Part I. Aqueous veins, Norman Ashton, *British Journal of Ophthalmology*, Vol. 35, pages 291-303, 1951.

casting, x-ray microcomputed tomography, fluorescein angiography, and vascular endothelial labeling techniques.¹ Of these, only SD-OCT imaging allows for noninvasive structural identification without contrast media, chemicals, or ionizing radiation. Further, without the need for corrosion, our method allows localization of the various components of the casting relative to the surrounding tissue by referring to

the corresponding structures within the 2D image stack (Fig. 3).

There was excellent agreement between structures visualized with SD-OCT and previous casting studies. Vascular morphological structures observed in this study (Figs. 10, 11) were compared to microcorrosion vascular castings in the published literature using either Microphil or neoprene studies

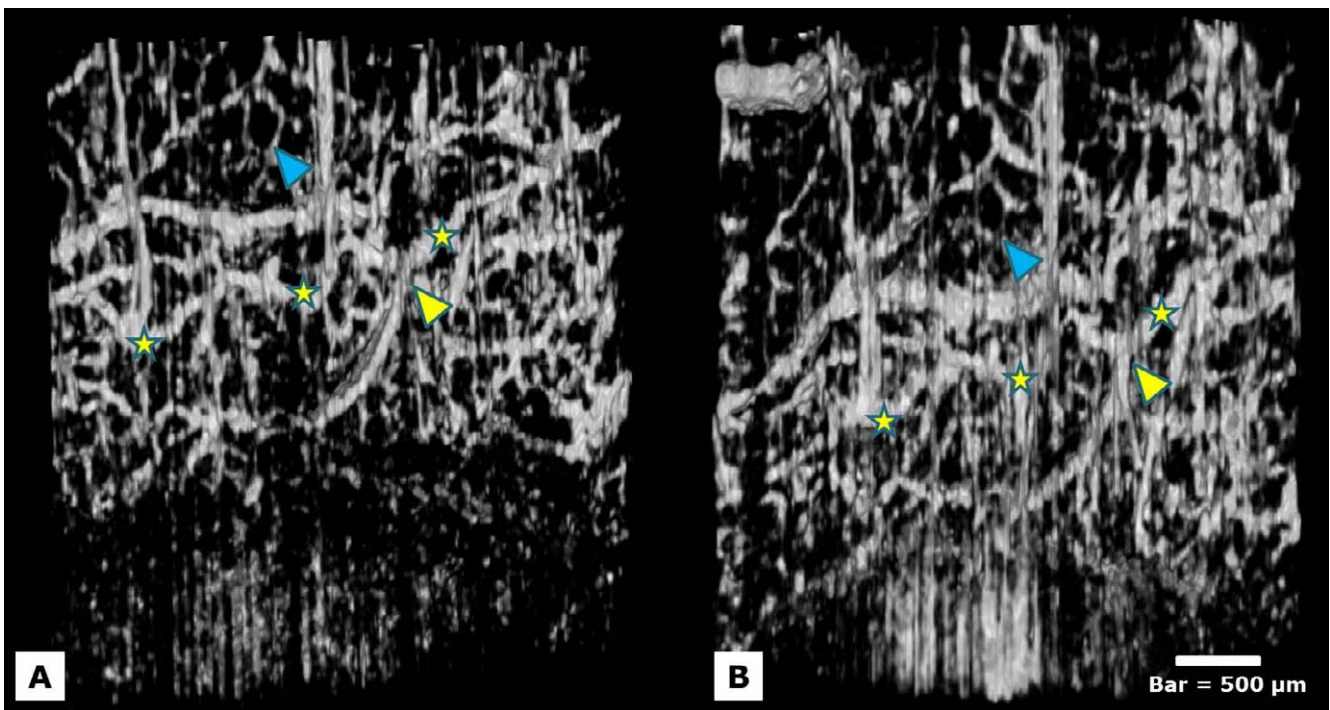


FIGURE 7. Two in vivo scans taken at separate times in the temporal quadrant of one individual are shown. The path of a tortuous vessel approximately 100 μm in diameter is shown (yellow stars). A site of anastomoses-conversion is indicated (yellow arrowhead). A venule between 20-40 μm in diameter is shown (blue arrowhead).

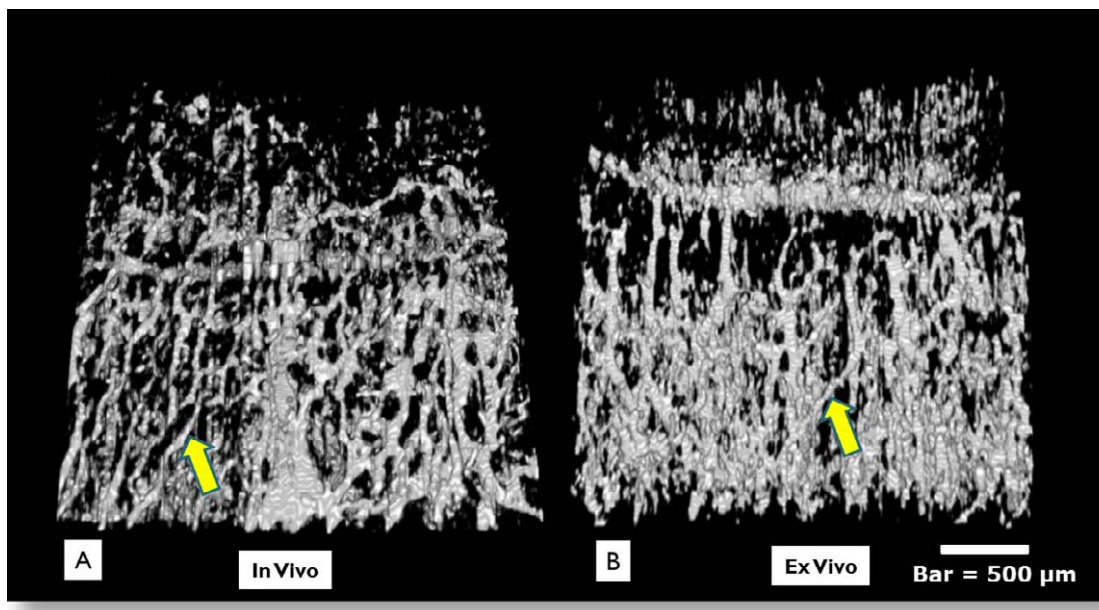


FIGURE 8. In vivo versus ex vivo virtual casting images are shown. Direct observations did not show marked differences in vivo (A) versus ex vivo (B). In vivo castings appeared to have a smaller vessel diameter, perhaps due to engorgement of vessels during perfusion ex vivo. In vivo castings are expected to also include arterial blood vessels, which are not active in the cadaver eye. Bar = 500 μ m.

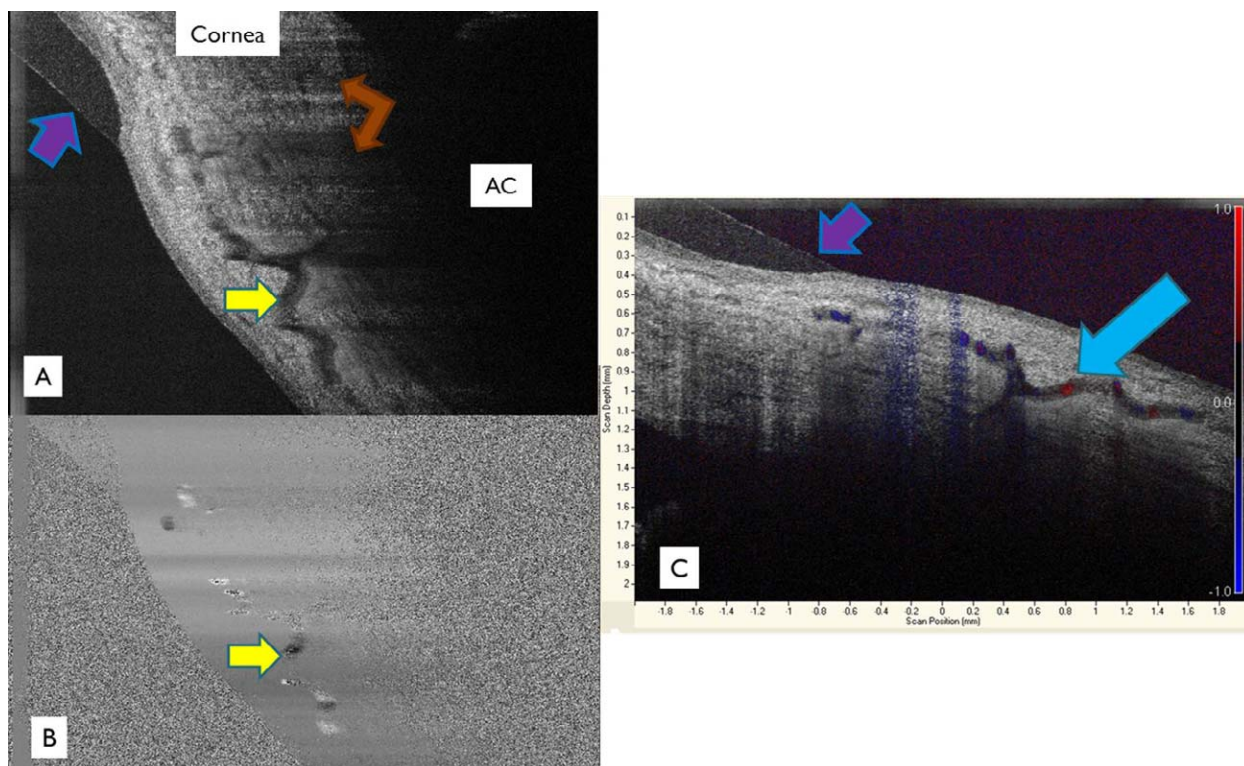


FIGURE 9. Doppler studies were performed on one eye in vivo to provide further evidence of venous outflow. (A) A large tortuous vein (yellow arrow) casts shadows towards the anterior chamber. Several aqueous venous shadows can be seen (brown arrows). A contact lens worn during this study is seen (purple arrows). (B) The vessel can be seen to have a characteristic laminar flow pattern, with slower flow near the edges of the vessel and more uniform flow near its center (blue arrow). Slow blood flow increases reflectance and mimics stationary tissue. (C) Color Doppler flow patterns are indicated and overlaid on top of a structural scan. Both blue and red flow patterns are seen in the same vessel due to the variable course of the vessel in relation to the SD-OCT scanner resulting in blood flowing towards and away from the probe at different areas. AC = anterior chamber.

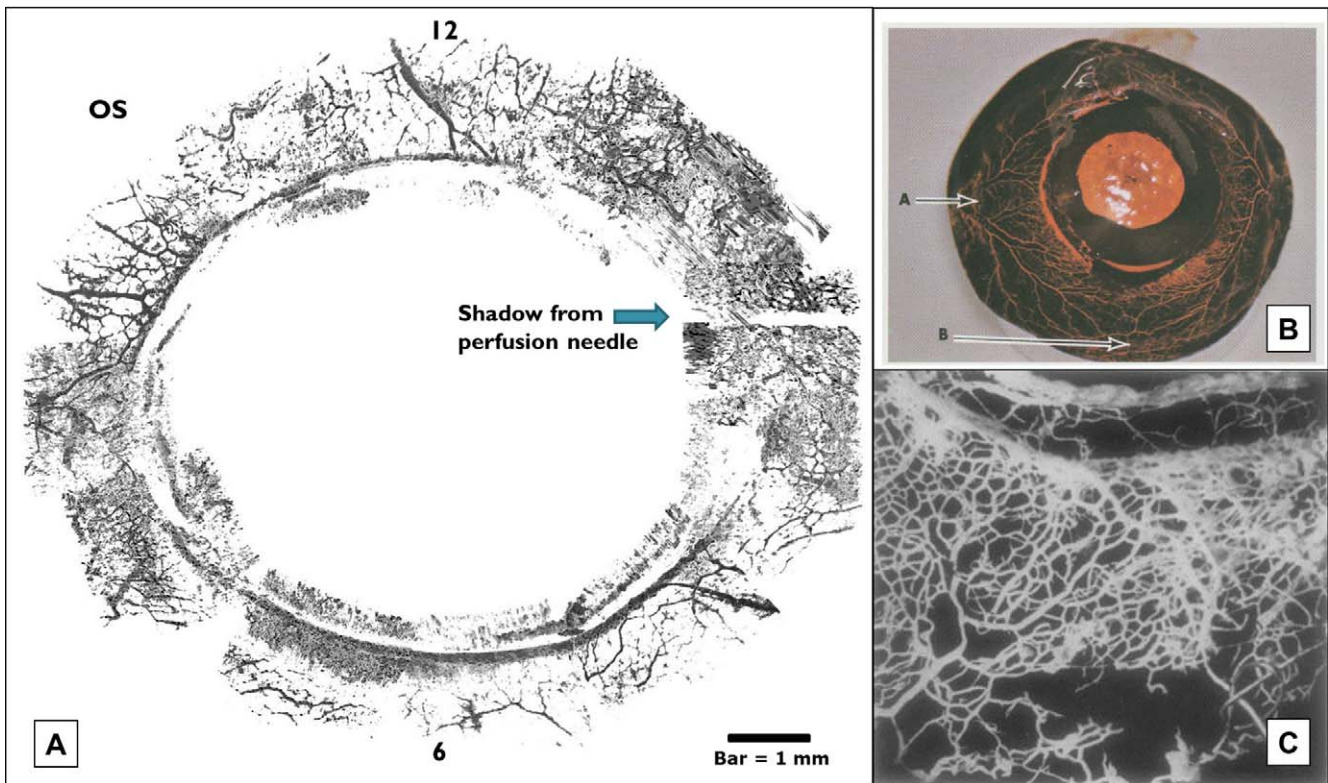


FIGURE 10. Close similarities were observed between 360-degree virtual castings (A) and previous studies using colored silicone casting agents in monkey eyes (B) and neoprene casting agents in human eyes (C). Note the dense array of vasculature in virtual castings compared to silicone and neoprene corrosion castings. Schlemm’s canal is seen as a discontinuous ring. OS = oculus sinister (left eye). Bar = 1 mm. Image (B) adapted with permission from Jocson VL, Sears ML. Channels of aqueous outflow and related blood vessels. II. Cercopithecus ethiops (Ethiopian green or green vervet). *Arch. Ophthalmol.* 1969;81:244-253; Image (C) adapted by permission from BMJ Publishing Group Ltd. Anatomical Study of Schlemm’s Canal and Aqueous Veins by means of Neoprene Casts: Part II. Aqueous Veins (continued), Norman Ashton, *British Journal of Ophthalmology*, Vol. 36, pages 265-267, 1952.

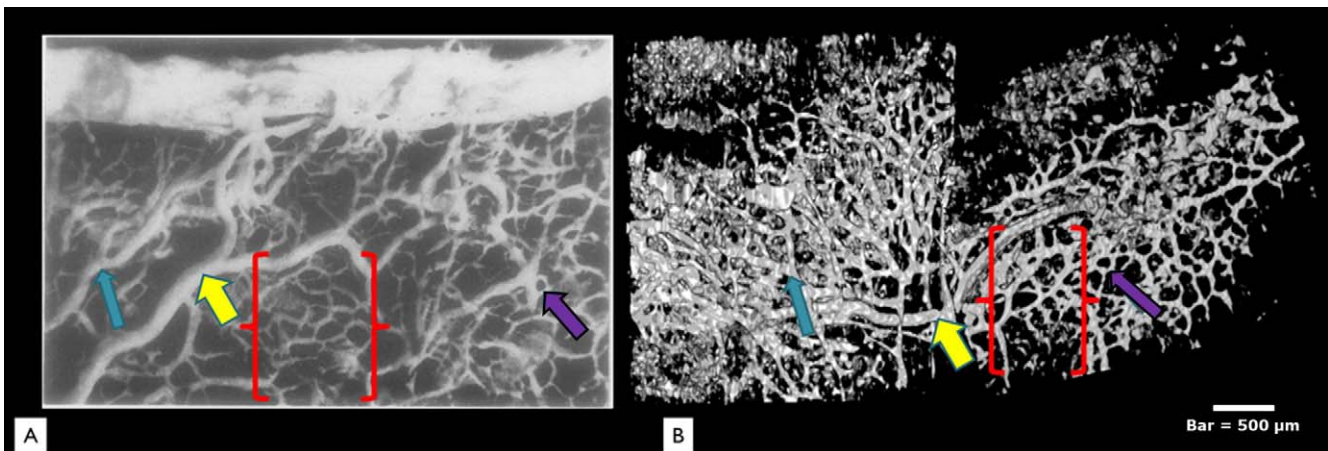


FIGURE 11. A high power view of a neoprene corrosion casting (A) is compared to a virtual casting using SD-OCT (B). All three major vessel types identified in this study were also seen in previous corrosion castings. A large tortuous vein, possibly an aqueous vein, is seen in both images draining vessels posterior from the limbus margin (yellow arrows). A mid-sized radial vessel is visualized (blue arrow). Small interconnecting venules (purple arrows) form a “hexagonal” meshwork (brackets) in both the neoprene casting and the SD-OCT virtual cast. Bar = 500 μm. Image adapted by permission from BMJ Publishing Group Ltd. Anatomical study of Schlemm’s canal and aqueous veins by means of neoprene casts: Part I. Aqueous veins, Norman Ashton, *British Journal of Ophthalmology*, Vol. 35, pages 291-303, 1951.

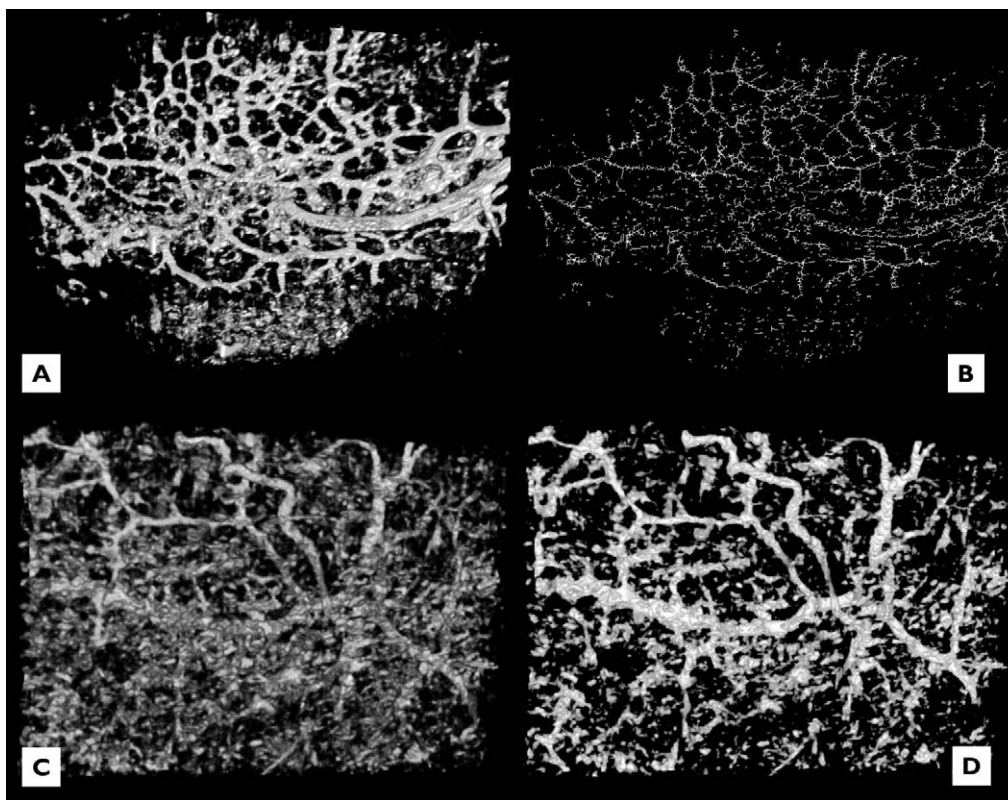


FIGURE 12. (A, B) A quantitative assessment of the number of vessels present was attempted using a function that skeletonized the images and made counting vessels manually easier, but a more precise algorithm is necessary. We have not yet determined the magnitude of the effect of processing on vessel diameter compared to raw images. (C, D) Noise that is removed in 2D cross-section cannot be distinguished definitely from vessel diameter. Three-dimensional data is necessary to confirm the identity of vessels and remove a sampling of cross-sectional measurements that include noise.

in humans,⁷⁻⁹ methyl methacrylate polymer resin studies with or without Mercox injected into blood vessels,²²⁻²⁹ or colored silicone.^{20,21} In the present study, perfusion with fluorescent microspheres was used for further confirmation that the virtual castings created with SD-OCT indeed isolate outflow microvasculature (Fig. 5). As with castings in the literature, there was excellent agreement between the microvasculature visualized in SD-OCT castings and that labeled by the microspheres.

Our SD-OCT hardware has a theoretical axial resolution of 1.3 μm ; however, vessels less than 10 μm were poorly observed. Nevertheless, we were able to track the vascular sources of the cast structures back to SC, suggesting that vessels of the smallest magnitude in the outflow vascular tree were visualized and were included in the casting. Vessels smaller than those present in our study, if present and connected to SC, may have collapsed post-mortem and were not reopened during perfusion due to the higher surface tension present in smaller vasculature.

In vivo vasculature appeared smaller and less distinct than ex vivo (Fig. 8). Ex vivo vasculature may also be artificially larger due to engorgement as part of the perfusion process, or small eye movement in vivo may be a factor.

We are confident that at least some structures we observed were venous vasculature comprising AH veins. By tracing vessels in the 2D stack, we could confirm that the smallest vessels connected directly to SC, and we have surrounding tissue in the slice to place the actual location of the vessels that we cast. The perfusion process allows venous structures to be enhanced more than arteries due to the preferential outflow through the conventional outflow system to the episcleral vasculature, which is principally a venous network.³⁰ Many

previous corrosion casting studies utilizing the conventional outflow system also confirm that the outflow vasculature is primarily venous, not arterial.^{20,21} Additionally, although the superficial limbus contains lymphatic vessels, which share some morphological similarities to venous networks, visualization of lymphatic vessels generally requires separate perfusion in the lymphatic system.¹

Using immunohistochemical studies, Selbach et al. identify arteriovenous anastomoses (AVA) and muscle-rich venules present in the episcleral vasculature.³¹ Quantitative evaluation of AVAs reported in this study included a density in the monkey (4–6/mm²) and in the human (0.5–1/mm²) episclera. They also describe a small artery adjacent to the outer wall of SC and branches of this artery leading directly into collector channels. If present in our study, any AVAs would be difficult to distinguish from normal venous anastomoses based on our SD-OCT processing schema. Further studies using Doppler combined with SD-OCT in vivo might suggest the presence of AVAs due to turbulent flow patterns from higher effective arterial pressure, although this would not be seen in the constant pressure-perfused cadaver model.

Doppler studies performed on one eye in vivo confirmed flow through a large tortuous venous structure (Fig. 9). The large Doppler signal visible in this vessel, compared to smaller signals in surrounding vasculature, suggest that this vessel is likely part of the blood flow system, possibly a terminal drainage vein in the aqueous outflow vascular tree. The vessel can be seen to have a characteristic laminar flow pattern, with slower flow near the edges of the vessel and more uniform flow near its center. Slow blood flow increases reflectance and mimics stationary tissue. Further studies using Doppler in vivo

may help differentiate blood vessels that comprise the AH vascular tree in the active circulatory system by drawing distinctions between morphology and flow characteristic of different vessel types.

Vascular density appears highest temporally, superiorly, and nasally in the virtual casting, with less dense arcades noted inferiorly. This closely resembled results from physical corrosion casting studies (Figs. 10, 11). The authors concede that, at present, there is no universally accepted method of quantifying vasculature structures in 3D SD-OCT virtual castings, so we cannot comment with absolute certainty that all vessels are being observed. Further methods of quantifying our findings, including tracer studies, histology, or paraffin sections, are needed to confirm whether preferential outflow based on density of vasculature exists in the human eye *ex vivo*. Ultimately, application of virtual castings will depend on determination of how each of these potential parameters is affected by the presence of glaucoma.

The unexpected observation of light and dark striations cannot be readily explained. This study was not designed to determine their source. Because of this observation, a new study exploring the textural features of the casting is under design.

Limitations of the study include the inability to distinguish arteries from veins as in stained sections, misinterpretation of noise for vessels, and the absence of a quantitative comparison of vessel number and vessel diameter. An assessment of the number of vessels present was attempted using a function that skeletonized the images and made counting vessels manually easier (Fig. 12), but developing a more precise algorithm proved to be a significant obstacle. In terms of measuring vessel size from SD-OCT images, the magnitude of the effect of processing on vessel diameter compared to raw images is not clear. Measurements made in 2D cross-section that are randomly distributed in space have the potential for error due to artificially high measurements from oblique cuts. Two-dimensional cross-section noise also cannot be distinguished definitely from vessel diameter. Three-dimensional data is necessary to confirm the identity of vessels and remove a sampling of cross-sectional measurements that include noise. These issues will be addressed in future work that will provide accurate quantification of cross-sectional diameters, but the purpose of the present qualitative study is the description of the presence of vascular meshwork structures in the outflow system that have not been previously described. A limitation of *in vivo* imaging includes eye movements. Although we created a custom mount, we could not completely eliminate these from our *in vivo* castings.

In conclusion, the first detailed morphometric analysis of small AH outflow structures obtained noninvasively *in situ* using SD-OCT is presented. Continued development of this technique may lead to clinically useful direct assessment of outflow in subjects with glaucoma.

References

- Van der Merwe EL, Kidson SH. Advances in imaging the blood and aqueous vessels of the ocular limbus. *Exp Eye Res.* 2010; 91:118-126.
- Gould DB, John SWM. Anterior segment dysgenesis and the developmental glaucomas are complex traits. *Hum Mol Genet.* 2002;11:1185-1193.
- Gould DB, Smith RS, John SWM. Anterior segment development relevant to glaucoma. *Int J Dev Biol.* 2004;48:1015-1029.
- Dvorak-Theobald G. Schlemm's canal: its anastomoses and anatomic relations. *Trans Am Ophthalmol Soc.* 1934;32:574-595.
- Dvorak-Theobald G. Further studies on the canal of Schlemm. *Am J Ophthalmol.* 1955;39:65-89.
- Ascher KW. Aqueous veins: physiologic importance of visible elimination of intraocular fluid. *Am J Ophthalmol.* 1942;25: 1174-1209.
- Ashton N. Anatomical study of Schlemm's canal and aqueous veins by means of neoprene casts, I: aqueous veins. *Br J Ophthalmol.* 1951;35:291-303.
- Ashton N. Anatomical study of Schlemm's canal and aqueous veins by means of neoprene casts, II: aqueous veins. *Br J Ophthalmol.* 1952;36:265-267.
- Ashton N, Smith R. Anatomical study of Schlemm's canal and aqueous veins by means of neoprene casts, III: arterial relations of Schlemm's canal. *Br J Ophthalmol.* 1953;37: 577-586.
- Irshad FA, Mayfield MS, Zurakowski D, Ayyala RS. Variation in Schlemm's canal diameter and location by ultrasound biomicroscopy. *Ophthalmology.* 2010;117:916-920.
- Kagemann L, Wollstein G, Ishikawa H, et al. Identification and assessment of Schlemm's canal by spectral-domain optical coherence tomography. *Invest Ophthalmol Vis Sci.* 2010;51: 4054-4059.
- Sarunic MV, Asrani S, Izatt JA. Imaging the ocular anterior segment with real-time, full-range Fourier-domain optical coherence tomography. *Arch Ophthalmol.* 2008;126:537-542.
- Rollins A, Yazdanfar S, Kulkarni M, Ung-Arunyawee R, Izatt J. *In vivo* video rate optical coherence tomography. *Opt Express.* 1998;3:219-229.
- Zhang K, Kang JU. Real-time 4D signal processing and visualization using graphics processing unit on a regular nonlinear-k Fourier-domain OCT system. *Opt Express.* 2010; 18:11772-11784.
- Kagemann L, Wollstein G, Ishikawa H, et al. 3D visualization of aqueous humor outflow structures *in-situ* in humans. *Exp Eye Res.* 2011;93(3):308-315.
- Ellingsen BA, Grant WM. The relationship of pressure and aqueous outflow in enucleated human eyes. *Invest Ophthalmol Vis Sci.* 1971;10:430-437.
- Bárány EH. Simultaneous measurement of changing intraocular pressure and outflow facility in the vervet monkey by constant pressure infusion. *Invest Ophthalmol Vis Sci.* 1964;3: 135-143.
- Erickson-Lamy K, Rohen JW, Grant WM. Outflow facility studies in the perfused human ocular anterior segment. *Exp Eye Res.* 1991;52:723-731.
- Cense B, Chen TC, Nassif N, et al. Ultra-high speed and ultra-high resolution spectral-domain optical coherence tomography and optical Doppler tomography in ophthalmology. *Bull Soc Belge Ophthalmol.* 2006;302:123-132.
- Jocson VL, Sears ML. Channels of aqueous outflow and related blood vessels, I: Macaca mulatta (rhesus). *Arch Ophthalmol.* 1968;80:104-114.
- Jocson VL, Sears ML. Channels of aqueous outflow and related blood vessels, II: Cercopithecus ethiops (Ethiopian green or green vervet). *Arch Ophthalmol.* 1969;81:244-253.
- Bhutto IA, Amemiya T. Microvasculature architecture of the rat choroid: corrosion cast study. *Anat Rec.* 2001;264:63-71.
- Morrison JC, Fraunfelder FW, Milne ST, Moore CG. Limbal microvasculature of the rat eye. *Invest Ophthalmol Vis Sci.* 1995;36:751-756.
- Ninomiya H, Kuno H. Microvasculature of the rat eye: scanning electron microscopy of vascular corrosion casts. *Vet Ophthalmol.* 2001;4:55-59.
- Ninomiya H, Inomata T, Kanemaki N. Microvascular architecture of the rabbit eye: a scanning electron microscopic study of vascular corrosion casts. *J Vet Med Sci.* 2008;70:887-892.

26. Ninomiya H, Inomata T. Microvasculature of the hamster eye: scanning electron microscopy of vascular corrosion casts. *Vet Ophthalmol.* 2005;8:7-12.
27. Ninomiya H, Inomata T. Microvascular anatomy of the pig eye: scanning electron microscopy of vascular corrosion casts. *J Vet Med Sci.* 2006;68:1149-1154.
28. Risco JM, Nopanitaya W. Ocular microcirculation. Scanning electron microscopic study. *Invest Ophthalmol Vis Sci.* 1980;19:5-12.
29. Van Buskirk EM. The canine eye: the vessels of aqueous drainage. *Invest Ophthalmol Vis Sci.* 1979;18:223-230.
30. Gaasterland DE, Jocson VL, Sears ML. Channels of aqueous outflow and related blood vessels. 3. Episcleral arteriovenous anastomoses in the rhesus monkey eye (*Macaca mulatta*). *Arch Ophthalmol.* 1970;84:770-775.
31. Selbach JM, Rohen JW, Steuhl KP, Lütjen-Drecoll E. Angioarchitecture and innervation of the primate anterior episclera. *Curr Eye Res.* 2005;30:337-344.